COMMUNICATION

Check for updates

Modulation of the assembly fashion among metal–organic frameworks for enantioretentive epoxide activation†

Jun Guo, [ID] *[a] Xiaomin Xue,[a] Fangfang Li,[a] Meiting Zhao, [ID] [b] Youcong Xing,[a] Yanmin Song,[c] Chang Long, [ID] [d] Tingting Zhao,[a] Yi Liu [ID] *[ae] and Zhiyong Tang [ID] *[d]

Highly enantioretentive alcoholysis of epoxides is an important way to synthesize enantiopure β-alkoxy alcohols, which are irreplaceable intermediates demanded by biomedicines, fine chemicals and other industries. In this report, we exploit a series of Zr-based metal–organic frameworks (Zr-MOFs) as the catalysts to achieve high activity and enantioretentivity in the alcoholysis of styrene oxide *via* modulating their assembly fashions. It is explored that hcp-UiO-66 not only exhibits a ∼10 fold improved catalytic activity than both hxl-CAU-26 and fcc-UiO-66 of varied assemblies but also maintains superior product enantioretentivity. Theoretic calculations together with experimental proof discloses the origin of distinct catalytic activity caused by different assembly fashions. This assembly modulation strategy offers a potential protocol for seeking high-performance catalysts among MOFs by virtue of their rich polymorphisms.

New concepts

As an emerging type of heterogeneous catalyst, metal–organic frameworks (MOFs) provide multiple freedoms for regulating catalytic performances usually through metal node variations, linker functionalizations, pore structure adjustments and defect engineering. Absolutely different from the above strategies, we report the modulation of the assembly fashions of MOF-based catalysts to implement double excellence in catalytic activity and product selectivity. As demonstrated by the performances acquired in the enantioretentive alcoholysis of epoxides, **hcp-UiO-66** with a hexagonal close-packed assembly fashion not only exhibits nearly 10-fold improved catalytic activity over the corresponding primitive hexagonal latticed **hxl-CAU-26** and face-centered cubic **fcc-UiO-66**, but also holds the highest product ee values. The great performance disparity is disclosed to originate from the assembly-dependent amount and charge distribution of active sites among polymorphic MOFs. The assembly modulation strategy reported in this work enables additional possibilities for seeking more high-performance MOF- or COF-based porous catalysts with both high conversion efficiency and product selectivity.

Introduction

Chirality is one of the basic attributes of nature. Specifically, basic building blocks like amino acids, saccharides and ribonucleic acids in life are all enantiopure chiral substances and rigorously comply with a specific set of chirality selection rules when performing their biological functionalities.[1–3] Thanks to vigorous advances of chiral science made in biomedicines,[4]

pesticides,[5,6] fine chemicals,[7] chiroptics,[8] and so on,[9] the increasing demand for various types of chiral substances in high enantiopurity has been an urgent task in chiral synthesis and asymmetric catalysis.[10–13] For instance, the enantioretentive alcoholysis of epoxide substrates is an important way to synthesize chiral β-alkoxy alcohols with 1,2-disynthons introduced, which are multifunctional chiral intermediates irreplaceable in preparations of chiral polyurethane elastomers, anticancer eugenol β-amino alcohols and derivatives.[14] However, owing to the poor nucleophilicity of alcohols, this reaction generally requires harsh conditions like high temperature, long reaction time and strong acid to get satisfactory conversions of epoxides.[15,16] Unfortunately, the worrisome racemization of chiral products will be prone to occur under harsh reaction conditions, while additional enantiomer separations and purifications have to be conducted prior to further usage. As a result, the catalytic activation of epoxides in both high activity and enantioretentivity is highly expected in order to gain

[a] *State Key Laboratory of Separation Membranes and Membrane Processes, School of Chemistry, Tiangong University, Tianjin 300387, China. E-mail: junguo@tiangong.edu.cn, yiliuchem@whu.edu.cn*

[b] *Tianjin Key Laboratory of Molecular Optoelectronic Sciences, Department of Chemistry, Institute of Molecular Aggregation Science, Tianjin University, Tianjin 300072, China*

[c] *Cosychem Technology (Tianjin) Co., Ltd, Tianjin 300457, China*

[d] *CAS Key Laboratory of Nanosystem and Hierarchical Fabrication, CAS Center for Excellence in Nanoscience, National Center for Nanoscience and Technology, Beijing 100190, China. E-mail: zytang@nanoctr.cn*

[e] *School of Chemical and Environmental Engineering, Wuhan Polytechnic University, Wuhan 430023, China*

† Electronic supplementary information (ESI) available. See DOI: https://doi.org/10.1039/d3nh00419h

enantiopure target products as well as save posttreatment costs, but still represents a grand challenge.[15–18]

As emerging crystalline porous materials, metal–organic frameworks (MOFs) have been widely recognized as efficient heterogeneous catalysts in versatile organic transformations, thanks to their abundant active sites, ordered pore structures, tuneable compositions and good thermal stabilities.[19–23] Notably, MOF-based catalysts have enabled the regulation of many catalytic reactions *via* metal node variation,[24,25] organic linker functionalization,[26,27] pore size adjustment,[28,29] and defect engineering.[30,31] For example, by changing the metal node from Zr to Hf, Hf-NU-1000 [$Hf_6(OH)_{16}(TBAPy)_2$, H_4TBAPy = 1,3,6,8-tetrakis(*p*-benzoic acid)pyrene] showed higher conversion rate than the isoreticular Zr-NU-1000 in the catalytic activation of epoxides due to its weaker Lewis acidity.[16] Moreover, defect engineering was recently proposed as a workable way for catalytic activity improvement.[32,33] Prototypes such as MOF-808 [$Zr_6O_4(CHOO)_6(BTC)_2$, BTC = 1,3,5-benzenetricarboxylate] featuring abundant linker defects exhibited excellent conversion and regioselectivity towards the ring-opening reaction of styrene oxide;[34] however, investigations about product enantioretentivity were rarely reported.

Beyond the aforementioned tricks in catalysis, in this work, we report the regulation of both catalytic activity and product enantioretentivity *via* modulating the assembly fashion among three typical Zr-MOFs. Those representatives are the primitive hexagonal latticed **hxl-CAU-26** [$Zr_6O_4(\mu_3\text{-OH})_4(BDC)_3(CH_3COO)_6$, BDC = 1,4-benzenedicarboxylate], hexagonal close-packed **hcp-UiO-66** [$Zr_{12}O_8(\mu_3\text{-OH})_8(\mu_2\text{-OH})_6(BDC)_9$], and face-centered cubic **fcc-UiO-66** [$Zr_6O_4(\mu_3\text{-OH})_4(BDC)_6$]. Note that the acetate modulator in **hxl-CAU-26** only serves as a coordination auxiliary and does not involve the corresponding assembly fashion. Depending on the assembly fashions, those Zr-MOFs show distinct catalytic conversions as well as product enantioretentivities in the alcoholysis of epoxides.

Results and discussion

Three types of Zr-MOFs with varied assembly fashion are selected and constructed according to previous reports with minor modifications (the synthesis details are available in the ESI†).[35–38] Among them, **hxl-CAU-26** MOF is composed of a 6-coordinated $Zr_6O_4(\mu_3\text{-OH})_4$ node and BDC linker *via* adopting the **hxl** network within the crystallographic *a*–*b* plane (Fig. 1a). Along the *c*-direction, as-formed 2D lamellas are further assembled into a 3D framework *via* the eclipsed AA stacking fashion (Fig. 1b). For the sake of charge balance, there are six additional acetate modulators occupied at the bottom and top of each metal node separately, thereby giving the formula of [$Zr_6O_4(\mu_3\text{-OH})_4(BDC)_3(CH_3COO)_6$] for **hxl-CAU-26**. The **hcp-UiO-66** MOF consists of $Zr_6O_4(\mu_3\text{-OH})_4$ dimer [$Zr_{12}O_8(\mu_3\text{-OH})_8(\mu_2\text{-OH})_6$] bridged by six μ_2-OH as the metal node (Fig. 1c), in which the 18-coordinated [$Zr_{12}O_8(\mu_3\text{-OH})_8(\mu_2\text{-OH})_6$] nodes linked by ditopical BDC linkers are assembled into a 3D **hcp** framework characteristic of the staggered AB stacking fashion (Fig. 1d).
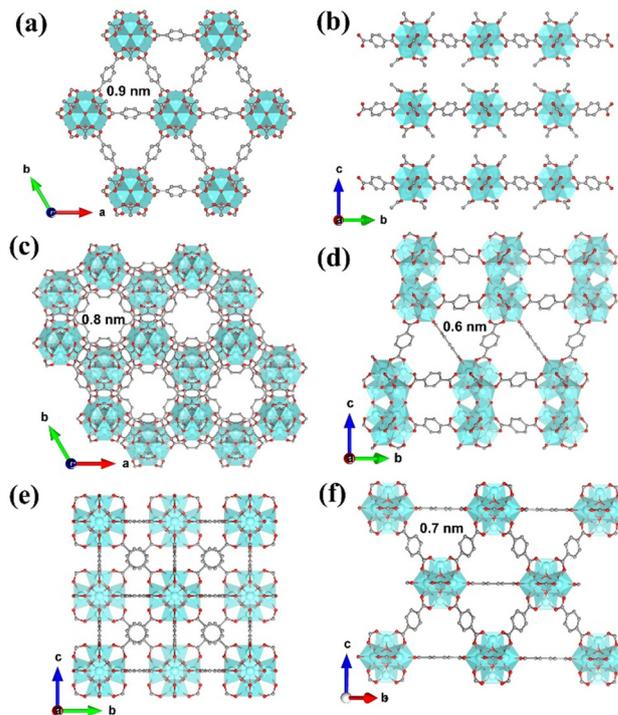

Fig. 1 (a) Crystallographic structure of **hxl-CAU-26** projected within the *a*–*b* plane. (b) Crystallographic structure of **hxl-CAU-26** assembled along the *c*-direction. (c) Crystallographic structure of **hcp-UiO-66** projected within the *a*–*b* plane. (d) Crystallographic structure of **hcp-UiO-66** assembled along the *b*–*c* plane. (e) Crystallographic structure of **fcc-UiO-66** projected within the *a*–*b* plane. (f) Crystallographic structure of **fcc-UiO-66** assembled along the *c*-direction.

Moreover, the classical **fcc-UiO-66** MOF is also constructed by connecting the 12-coordinated [$Zr_6O_4(\mu_3\text{-OH})_4$] metal node with BDC linkers, which is characteristic of a 3D **fcc** topology with the ABC assembly fashion (Fig. 1e and f).

According to the scanning electron microscope (SEM) image, one can see the successful construction of lamellar-shaped **hxl-CAU-26** MOF with an averaged lateral size of 1.1 μm (Fig. 2a and Fig. S1a, ESI†). Its experimental powder X-ray diffraction (PXRD) pattern well correlates with the simulated one, with the first three diffraction peaks assigned to the (001), (100), and (110) facets in sequence (Fig. 2b). The **hcp-UiO-66** MOF is also characteristic of the hexagonal plate morphology and shaped in a larger lateral size of 2.9 μm than **hxl-CAU-26** (Fig. 2c and Fig. S1b, ESI†). In addition, the sharp diffraction peaks of **hcp-UiO-66** also match with the simulation result, indicating its high crystallinity free of impurity phase (Fig. 2d). Differently, the **fcc-UiO-66** MOF shows a characteristic (111)-exposed octahedral morphology with an averaged particle size of 5.8 μm (Fig. 2e and Fig. S1c, ESI†). Its high extinction PXRD pattern featured with the main (111) and (200) peaks further confirms the successful construction of the **fcc-UiO-66** phase (Fig. 2f). Transmission electron microscopy (TEM) imaging and electron diffraction (ED) are further carried out on three types of MOFs, which also show consistent results with the corresponding structure simulations (Fig. S3–S5, ESI†).
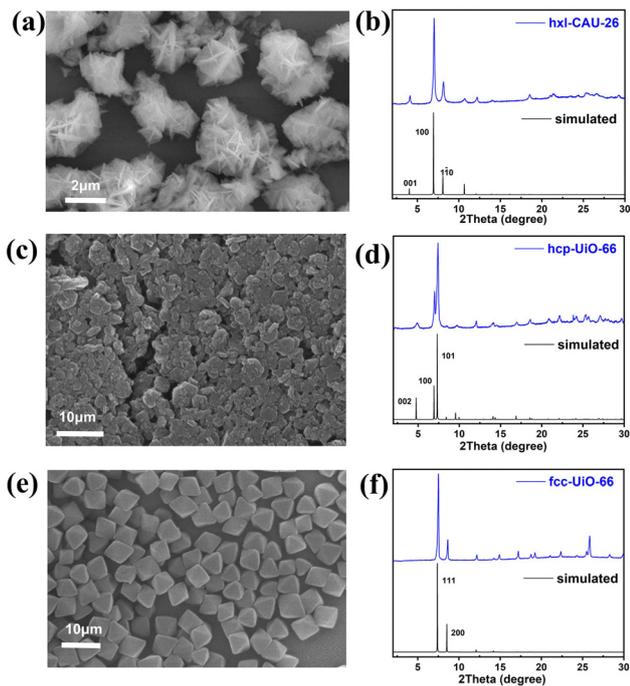
Fig. 2 (a) SEM image and (b) PXRD pattern of **hxl-CAU-26**, (c) SEM image and (d) PXRD pattern of **hcp-UiO-66**, (e) SEM image and (f) PXRD pattern of **fcc-UiO-66**.

Besides, Fourier transform infrared (FT-IR) spectra demonstrate the effective removal of residual H_2BDC ligands inside the corresponding MOF pores (Fig. S2, ESI†), which are accessible for further evaluation.

The N_2 adsorption and desorption of three types of Zr-MOFs (**hxl-CAU-26**, **hcp-UiO-66**, and **fcc-UiO-66**) are recorded at 77 K. As shown in Fig. S6 (ESI†), type I adsorption isotherms are discerned for **hxl-CAU-26**, **hcp-UiO-66** and **fcc-UiO-66** with the Brunauer–Emmett–Teller (BET) specific surface areas of 674.1 $m^2 g^{-1}$, 327.1 $m^2 g^{-1}$ and 876.5 $m^2 g^{-1}$, respectively. In addition to populations of crystallographic micropores (Fig. 1), pore size distribution (PSD) curves of **hcp-UiO-66** and **fcc-UiO-66** present 1.3–1.4 nm pore populations in Fig. 3a, indicating the existence of defective pores raised from missing linkers. Thermogravimetric analyses (TGA) also confirmed linker
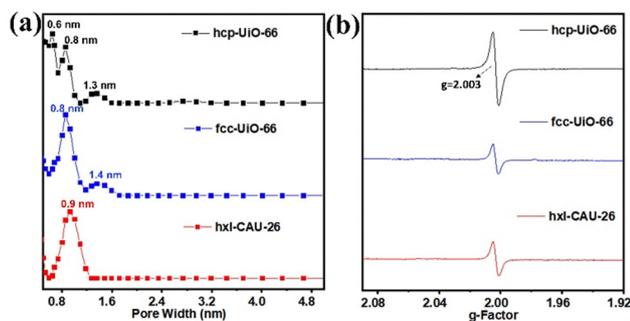

Fig. 3 (a) Pore size distribution of **hcp-UiO-66**, **fcc-UiO-66** and **hxl-CAU-26** according to the N_2-DFT method. (b) EPR spectra of **hcp-UiO-66**, **fcc-UiO-66** and **hxl-CAU-26**.

defects in both **hcp-UiO-66** and **fcc-UiO-66**, according to their much lower BDC linker proportions than the theoretical ones (Fig. S7, ESI†). Moreover, the quantitative defect number of **hcp-UiO-66** and **fcc-UiO-66** is estimated to be 8.6 per $[Zr_{12}O_8(\mu_3\text{-}OH)_8(\mu_2\text{-}OH)_6]$ node and 5.4 per $[Zr_6O_4(\mu_3\text{-}OH)_4]$ node, respectively (Table S1, ESI†). As a comparison, **hxl-CAU-26** presents an inherent 6 linker defects per node based on its crystallographic formula of $Zr_6O_4(BDC)_3(CH_3COO)_6$, as verified by the coincident BDC loss between experimental and theoretical ones (Table S1, ESI†). The above defect evaluations among MOFs are further validated by electron paramagnetic resonance (EPR) spectroscopy. As shown in Fig. 3b, the three types of Zr-MOFs all display strong isotropic EPR signals with the same g-factor of 2.003, a characteristic indicator of defect-induced oxygen vacancies.[39] In line with the TGA results, the EPR signal of **hcp-UiO-66** gives a spin count up to 6.41×10^{17} spins g^{-1}, which is considerably higher than that of both **hxl-CAU-26** (3.53×10^{17} spins g^{-1}) and **fcc-UiO-66** (3.23×10^{17} spins g^{-1}).

Bearing defect-induced metal sites, the above Zr-MOFs with varied assembly fashion are tested as Lewis acid catalysts in the alcoholysis of epoxides. As outlined in Table 1, **hcp-UiO-66** MOF achieved nearly 100% conversion in the methanolysis of (S)-styrene oxide at 30 °C and within only 4 h (Entry 1). Benefitting from the very mild reaction temperature and short reaction time, 96.2% enantiomeric excess (ee) of 2-methoxy-2-phenyl-ethan-1-ol product is maintained in comparison to the 97% ee of the initial substrate.

In sharp contrast, **fcc-UiO-66** and **hxl-CAU-26** present only ∼10% conversions and the homogeneous $ZrCl_4$ fails to show any catalytic activity under the otherwise identical reaction conditions (Table S2, ESI†). Accordingly, harsher reaction

Table 1 Catalytic summary and comparison of three Zr-MOF catalysts in enantioretentive alcoholysis of styrene oxide

Entry	Sub.1	Sub.2	Catalyst	T/°C	t/h	Con./%	ee/%
1	$S_1{}^a$	$S_2{}^a$	**hcp**	30	4	99.9	96.2
2	$S_1{}^a$	$S_2{}^a$	**fcc**	80	48	93.6	91.3
3	$S_1{}^a$	$S_2{}^a$	**hxl**	80	48	96.4	93.5
4	$S_1{}^b$	$S_2{}^a$	**hcp**	30	4	94.0	95.8
5	$S_1{}^b$	$S_2{}^a$	**fcc**	80	48	91.8	84.8
6	$S_1{}^b$	$S_2{}^a$	**hxl**	80	48	92.5	87.8
7	$S_1{}^a$	$S_2{}^b$	**hcp**	60	48	97.0	94.8
8	$S_1{}^a$	$S_2{}^b$	**fcc**	100	72	84.6	91.1
9	$S_1{}^a$	$S_2{}^b$	**hxl**	100	72	93.3	91.9
10	$S_1{}^b$	$S_2{}^b$	**hcp**	60	48	96.3	96.1
11	$S_1{}^b$	$S_2{}^b$	**fcc**	100	72	90.3	85.1
12	$S_1{}^b$	$S_2{}^b$	**hxl**	100	72	91.1	86.8

The reaction conditions of enantioretentive alcoholysis: 2 mg catalyst, 28.5 μL of substrate 1 and 5 mL of substrate 2 were mixed into a 15 mL glass flask to react at a certain temperature for a certain time.
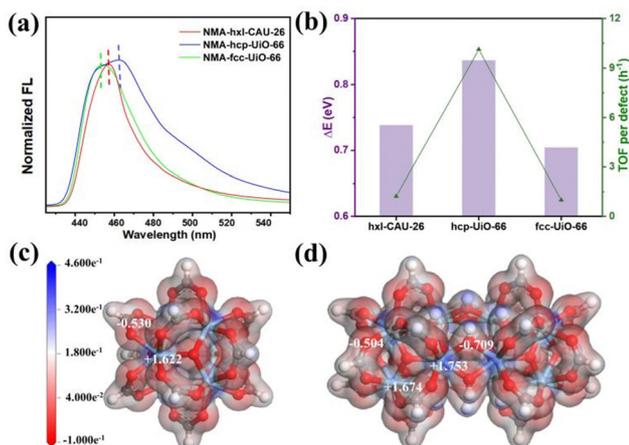
Fig. 4 (a) Fluorescence spectra of NMA binding to **hxl-CAU-26**, **hcp-UiO-66** and **fcc-UiO-66** in CH_3CN. (b) The correlation between ΔE and TOF per defect among **hxl-CAU-26**, **hcp-UiO-66** and **fcc-UiO-66**. The charge density distribution profiles of $Zr_6O_4(\mu_3\text{-OH})_4$ in both **hxl-CAU-26** and **fcc-UiO-66** node (c) and (d) $Zr_{12}O_8(\mu_3\text{-OH})_8(\mu_2\text{-OH})_6$ in **hcp-UiO-66**.

conditions (80 °C for 48 h) are required to get high substrate conversions (entries 2 and 3). Unfortunately, the product ee values consequently decrease to 91.3% and 93.5% for **fcc-UiO-66** and **hxl-CAU-26**, respectively, caused by accelerated racemizations under harsh conditions. Similarly, the performances taken by using (*R*)-styrene oxide as the substrate also give inferior ee values for **fcc-UiO-66** and **hxl-CAU-26** compared with that of **hcp-UiO-66** (entries 4–6). To further demonstrate both superior conversion activity and enantioretentivity of **hcp-UiO-66**, ethanol of weaker nucleophilicity is used in replacement of methanol for the addition of styrene oxide (entries 7–12). One can see that **hcp-UiO-66** gives conversion over 95% and product ee of 94.8% at 60 °C for 48 h. The comparable substrate conversions are gained by **fcc-UiO-66** and **hxl-CAU-26** at raised temperature (100 °C) and prolonged reaction time (72 h), but at the cost of reduced product ee values.

The best performances achieved by **hcp-UiO-66** are intuitively associated most with its highest defect amount among the three types of Zr-MOFs, as disclosed by both TGA and EPR characterizations (Fig. 3b and Table S1, ESI†). Similarly, the superior performance of **hxl-CAU-26** over **fcc-UiO-66** is also ascribed to the higher defect amount in the former. Besides, the inherent catalytic activity (*i.e.* Lewis acidity) of each metal site may also vary among Zr-MOFs of varied assembly fashion. Hence, the *N*-methylacridone (NMA)-based fluorescent probe is used to distinguish the Lewis acidity disparity of metal sites among MOFs.[34,40–42] Initially, the free NMA probe shows a blue emission in CH_3CN with the maximum peak wavelength (λ_{max}) centered at 433.0 nm (Fig. S13, ESI†). Upon binding to metal sites among MOFs, the emission of NMA undergoes a redshift with a positive relationship to the binding energy (ΔE) between NMA and MOFs. As shown in Fig. 4a, the initial λ_{max} changes significantly from 433.0 nm to 455.2 nm, 457.4 nm and 463.8 nm after binding to **fcc-UiO-66**, **hxl-CAU-26** and **hcp-UiO-66**, respectively. The largest ΔE of 0.836 eV is therefore

obtained for **hcp-UiO-66**, meaning the highest catalytic activity of the corresponding metal site. Furthermore, we calculate the turnover frequency based on each defect site (TOF per defect) for three Zr-MOFs of varied assembly fashions (Table S2, ESI†). Remarkably, the highest TOF per defect (up to 10.1 h^{-1}) is offered by hcp-UiO-66 while **fcc-UiO-66** and **hxl-CAU-26** provided only 1.0 h^{-1} and 1.2 h^{-1} TOF per defect, respectively. Meanwhile, a consistent correlation between the TOF per defect with ΔE of each type of MOF is found in Fig. 4b. These results clearly uncover the assembly fashion-varied catalytical activity, especially between the **hcp** one and the others.

Scrutiny on the example of **hcp-UiO-66** figures out an additional shoulder peak (455.0 nm) close to the peak position of **fcc-UiO-66**, an indication of two different Zr sites in the **hcp** assembly scaffold. To get an in-depth understanding, we then calculate the charge density distribution of the Zr sites among three assembly types. As both **hxl-CAU-26** and **fcc-UiO-66** share the same node, there are only $Zr_6O_4(\mu_3\text{-OH})_4$ (Fig. 4c) and $Zr_{12}O_8(\mu_3\text{-OH})_8(\mu_2\text{-OH})_6$ (Fig. 4d) nodes taken as theoretical moderns for consideration. As displayed in Fig. 4c, each Zr site in $Zr_6O_4(\mu_3\text{-OH})_4$ for both **hxl-CAU-26** and **fcc-UiO-66** is identically coordinated with 4 carboxylate oxygens and 4 μ_3-OH, which presents a positive charge of +1.622 according to the Mulliken population analysis. In comparison, two distinct types of Zr site are clearly found for $Zr_{12}O_8(\mu_3\text{-OH})_8(\mu_2\text{-OH})_6$ in **hcp-UiO-66** (Fig. 4d). Except for one same coordination as $Zr_6O_4(\mu_3\text{-OH})_4$, the other type of Zr site appears as replacing 2 carboxylate oxygens with 2 bridged μ_2-OH. Impressively, the latter Zr site obviously shows a higher Mulliken charge up to +1.753 due to the stronger electronegativity of μ_2-OH than the carboxylate group, which is on account of the congenitally higher activity of **hcp-UiO-66** over both **hxl** and **fcc** ones.

Conclusions

In summary, three types of Zr-MOFs including **hxl-CAU-26**, **hcp-UiO-66** and **fcc-UiO-66** with varied assembly fashion are adopted to regulate the catalytic performances in the alcoholysis of epoxides. Taking advantage of a much higher proportion of linker defect and inherently stronger activation capability, **hcp-UiO-66** not only exhibits nearly 10-fold TOF per node compared to both **hxl-CAU-26** and **fcc-UiO-66** but also maintains superior product enantioretentivity. The assembly-dependent performances found in this work enlighten an alternative way, namely tuning the polymorphism of MOFs, for driving more organic transformations in both high conversion efficiency and product selectivity.

Experimental

Experimental details and supplementary figures can be found in the ESI.†

Conflicts of interest

There are no conflicts to declare.

Acknowledgements

Notes and references

1 W. Gong, Z. Chen, J. Dong, Y. Liu and Y. Cui, *Chem. Rev.*, 2022, **122**, 9078–9144.

2 J. Liang, A. Hao, P. Xing and Y. Zhao, *ACS Nano*, 2021, **15**, 5322–5332.

3 J. Guo, Y. Zhang, Y. Zhu, C. Long, M. Zhao, M. He, X. Zhang, J. Lv, B. Han and Z. Tang, *Angew. Chem., Int. Ed.*, 2018, **57**, 6873–6877.

4 F. Wang, X. Yue, Q. Ding, H. Lin, C. Xu and S. Li, *Nanoscale*, 2023, **15**, 2541–2552.

5 S. Gómez Graña, J. Pérez Juste and P. Hervés, *Adv. Colloid Interface Sci.*, 2021, **288**, 102338.

6 X. Zhang, Z. Wang, X. Huang, Q. Huang, Y. Wen, B. Li, M. Holmes, J. Shi and X. Zou, *Chem. Eng. J.*, 2023, **451**, 138928.

7 P. Barbaro, V. Dal Santo and F. Liguori, *Dalton Trans.*, 2010, **39**, 8391–8402.

8 N. H. Cho, A. Guerrero Martínez, J. Ma, S. Bals, N. A. Kotov, L. M. Liz Marzán and K. T. Nam, *Nat. Biomed. Eng*, 2023, **1**, 88–106.

9 L. Zhang, H. X. Wang, S. Li and M. Liu, *Chem. Soc. Rev.*, 2020, **49**, 9095–9120.

10 Q. Han, B. Qi, W. Ren, C. He, J. Niu and C. Duan, *Nat. Commun.*, 2015, **6**, 10007.

11 H. Liu, H. Li, Y. He, P. Cheng, Y. Q. Zhang, B. Feng, H. Li, K. Wu and L. Chen, *Nat. Commun.*, 2023, **14**, 2100.

12 N. Antil, N. Akhtar, R. Newar, W. Begum, A. Kumar, M. Chauhan and K. Manna, *ACS Catal.*, 2021, **11**, 10450–10459.

13 J. Guo, Y. Wan, Y. Zhu, M. Zhao and Z. Tang, *Nano Res.*, 2020, **14**, 2037–2052.

14 C. Teixeira, R. B. Pereira, N. F. S. Pinto, C. M. M. Coelho, M. J. G. Fernandes, A. G. Fortes, M. S. T. Goncalves and D. M. Pereira, *Int. J. Mol. Sci.*, 2022, **23**, 3759.

15 K. Berijani and A. Morsali, *J. Catal.*, 2019, **378**, 28–35.

16 H. Beyzavi, R. C. Klet, S. Tussupbayev, J. Borycz, N. A. Vermeulen, C. J. Cramer, J. F. Stoddart, J. T. Hupp and O. K. Farha, *J. Am. Chem. Soc.*, 2014, **136**, 15861–15864.

17 Y. Gu, B. A. Anjali, S. Yoon, Y. Choe, Y. G. Chung and D. W. Park, *J. Mater. Chem. A*, 2022, **10**, 10051–10061.

18 X. Chen, Z. Qiao, B. Hou, H. Jiang, W. Gong, J. Dong, H. Li, Y. Cui and Y. Liu, *Nano Res.*, 2020, **14**, 466–472.

19 Y. Zhao, S. Qi, Z. Niu, Y. Peng, C. Shan, G. Verma, L. Wojtas, Z. Zhang, B. Zhang, Y. Feng, Y. S. Chen and S. Ma, *J. Am. Chem. Soc.*, 2019, **141**, 14443–14450.

20 O. Yang, X. Gao, G. Qi, Y. Wang, W. Dong, Z. Tian, J. Zhao, D. Li and Q. Zhang, *ACS Appl. Energy Mater.*, 2022, **6**, 334–341.

21 J. Guo, C. Yang and Y. Zhao, *Acc. Chem. Res.*, 2022, **55**, 1160–1170.

22 C. Yang, J. Yu, L. Zhai, S. Jia, T. Yang, W. Xiong and Q. Zhang, *Chem. Eng. J.*, 2023, **467**, 143511.

23 J. Guo, Y. Qin, Y. Zhu, X. Zhang, C. Long, M. Zhao and Z. Tang, *Chem. Soc. Rev.*, 2021, **50**, 5366–5396.

24 H. Wang, M. Gu, X. Huang, A. Gao, X. Liu, P. Sun and X. Zhang, *J. Mater. Chem. A*, 2023, **11**, 7239–7245.

25 A. H. Valekar, M. Lee, J. W. Yoon, J. Kwak, D. Y. Hong, K. R. Oh, G. Y. Cha, Y. Kwon, J. Jung, J. Chang and Y. Hwang, *ACS Catal.*, 2020, **10**, 3720–3732.

26 T. Y. Zhou, B. Auer, S. J. Lee and S. G. Telfer, *J. Am. Chem. Soc.*, 2019, **141**, 1577–1582.

27 C. Tan, X. Han, Z. Li, Y. Liu and Y. Cui, *J. Am. Chem. Soc.*, 2018, **140**, 16229–16236.

28 Y. H. Hu, C. X. Liu, J. C. Wang, X. H. Ren, X. Kan and Y. B. Dong, *Inorg. Chem.*, 2019, **58**, 4722–4730.

29 J. Li, P. M. Bhatt, J. Li, M. Eddaoudi and Y. Liu, *Adv. Mater.*, 2020, **32**, 2002563.

30 Q. Fu, D. Liu, W. Niu, S. Zhang, R. Chen, Y. Wang, P. Zhao, H. Jiang, Y. Zhao, L. Yang, L. Yan, H. Wang and X. Zhao, *Fuel*, 2022, **327**, 125085.

31 X. Feng, H. S. Jena, C. Krishnaraj, K. Leus, G. Wang, H. Chen, C. Jia and P. Van Der Voort, *ACS Appl. Mater. Interfaces*, 2021, **13**, 60715–60735.

32 Z. Niu, W. Zhang, P. C. Lan, B. Aguila and S. Ma, *Angew. Chem., Int. Ed.*, 2019, **58**, 7420–7424.

33 X. Rong, H. J. Wang, X. L. Lu, R. Si and T. B. Lu, *Angew. Chem., Int. Ed.*, 2020, **59**, 1961–1965.

34 P. Ji, X. Feng, P. Oliveres, Z. Li, A. Murakami, C. Wang and W. Lin, *J. Am. Chem. Soc.*, 2019, **141**, 14878–14888.

35 L. Zhou, S. Wang, Y. Chen and C. Serre, *Microporous Mesoporous Mater.*, 2019, **290**, 109674.

36 S. Leubner, H. Zhao, N. Van Velthoven, M. Henrion, H. Reinsch, D. E. De Vos, U. Kolb and N. Stock, *Angew. Chem., Int. Ed.*, 2019, **58**, 10995–11000.

37 Y. Wu, X. Wang, K. O. Kirlikovali, X. Gong, A. Atilgan, K. Ma, N. M. Schweitzer, N. C. Gianneschi, Z. Li, X. Zhang and O. K. Farha, *Angew. Chem., Int. Ed.*, 2022, **61**, e202117528.

38 K. Momma and F. Izumi, *J. Appl. Crystallogr.*, 2011, **44**, 1272–1276.

39 R. Xu, Q. Ji, P. Zhao, M. Jian, C. Xiang, C. Hu, G. Zhang, C. Tang, R. Liu, X. Zhang and J. Qu, *J. Mater. Chem. A*, 2020, **8**, 7870–7879.

40 Y. Quan, G. Lan, W. Shi, Z. Xu, Y. Fan, E. You, X. Jiang, C. Wang and W. Lin, *Angew. Chem., Int. Ed.*, 2021, **60**, 3115–3120.

41 K. Ohkubo, S. C. Menon, A. Orita, J. Otera and S. Fukuzumi, *J. Org. Chem.*, 2003, **68**, 4720–4726.

42 P. Ji, T. Drake, A. Murakami, P. Oliveres, J. H. Skone and W. Lin, *J. Am. Chem. Soc.*, 2018, **140**, 10553–10561.